UDC 001.1(082)
DOI: 10.15587/1729-4061.2019.164232

INVESTIGATION OF COGGING FORCES USING RELUCTANCE CIRCUITS EQUIVALENT APPROXIMATION IN A LADDER SECONDARY SINGLE-SIDED LINEAR INDUCTION MOTOR

Mochammad Rusli
Doctoral student*
E-mail: rusli@ub.ac.id
I. N. G. Wardana
PhD, Professor*
E-mail: wardana@ub.ac.id
Moch Agus Choiron
Doctor of Technical Sciences, Associate Professor*
E-mail: agus_choiron@ub.ac.id
Muhammad Aziz Muslim
Doctor of Technical Sciences, Associate Professor**
E-mail: muh_aziz@ub.ac.id
*Department of Mechanical Engineering***
Department of Electrical Engineering*
***Brawijaya University
Jalan. Mayjend Haryono, 167, Malang, Indonesia, 65145

Лінійні асинхронні двигуни останнім часом відіграють важливу роль в позиціонуванні лінійного руху. Однак вони мають низький рівень точності для застосування дуже низьких швидкостей. Для підвищення чіткості ЛАД, особливо при застосуванні дуже низьких швидкостей – високопродуктивний двигун – наявність сил зчеплення за рахунок зміни магнітної провідності повітряного зазору або інтерактивної зміни магнітного поля і крайового ефекту в односторонньому лінійному асинхронному двигуні з багатоланковим вторинним елементом (ЛАДБВЕ) має бути зменшено. У даному дослідженні розроблені дві прості магнітні ланцюги: одно- і багатослотова модель. Аналіз сил зчеплення пов'язаний зі зміною магнітної енергії в повітряному зазорі. Ґрунтуючись на магнітній провідності в паралельних і послідовних структурах, аналіз ЕСЛ виконується шляхом реалізації першого і другого закону Кірхгофа. Показано, що аналітичні результати близькі до результатів експериментів і програмного забезпечення методу скінченних елементів. В роботі дається прогноз замкнутої математичної моделі максимальних сил зчеплення для односторонніх лінійних асинхронних двигунів. Таким чином, дані результати можуть внести вклад в розробку фізичного одно- або двостороннього лінійного асинхронного двигуна. Зміна щільності потоку в повітряному зазорі в середній області ЛАДБВЕ може бути використана при розрахунку сил зчеплення, а зміна полів шляху магнітного потоку в крайовій області може зменшити величину щільності потоку в повітряному зазорі, але сили зчеплення в крайовій області можуть нейтралізувати одна одну

Ключові слова: лінійний асинхронний двигун, сили зчеплення, ланцюг опору, електромагнітне поле

1. Introduction

Nowadays, high-precision stages are required in many fields such as semiconductor industry, precision machining tools, data storage equipment and so on [1]. The systems must have high performance, such as high precision and slow speed. Ever-increasing requirements for higher productivity and better product quality in advanced manufacturing industries, such as the semiconductor and precision engineering industries, have continued to motivate and stimulate the development of high-speed and high-precision motion control systems. The one limiting factor in designing linear induction motor for obtaining its linear movement precisely is cogging forces [2].

Due to the cogging forces of ladder secondary linear induction motors have a high nonlinear characteristic, the prediction of cogging forces using the one dimension field method can not estimate the cogging forces precisely [3]. Cogging force can be calculated by electromagnetic finite element analysis (FEA). However, the finite element method for calculation of the cogging forces is relatively time-consuming, and is not appropriate for determining their optimal dimensions so as to minimize cogging [Zhu]. In order to increase the precision of the method, the two-dimensional field (2D-3D) method has been also developed in the prediction of cogging forces. However, this method is complicated and time-consuming [4].

The other prediction method is using flux-MMF diagram technique. It offers a fundamental graphics concept, approved as a basis of graphics design evaluation and a clear physical insight [5]. However, the graphic method compared with the numeric method is still more precise using the finite element method. The cogging forces can be predicted by seeing a stored magnetic energy variation in the air gap. It is based on the concept that a linear induction motor with ladder secondary results from the position-varying magnetic pressure (attractive forces) [6].

Therefore, the development of an easy cogging force prediction using the one-dimensional field supported with the reluctance network equivalent is relevant. Since using the Kirchoff law, determination of cogging forces in the air gap can be done straightaway. Also, the calculation process of this method is not time-consuming. For any particular linear induction motor, there is a great possibility to construct a magnetic circuit which represents it with a certain level of accuracy. For simplicity, it would be assumed that

all the sections of iron were magnetic short circuits (nodes) and that the air gaps separating the moving and stationary parts can be represented into linear reluctances which can be calculated by well-known laws. This circuit would then behave like a linear resistive electrical network and its solution would be found straightforward by using Kirchhoff laws.

2. Literature review and problem statement

The one problem of designing a ladder secondary double-sided linear induction motor for precision movement purposes is the existence of cogging forces [7]. In order to reject the cogging force as small as possible, it required the mathematical expression that represents the relationship between cogging forces with the geometrical dimensions of motor [8]. Fig. 1 shows the physical designed double-sided linear induction motor.

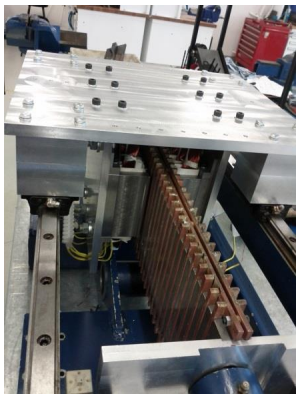

Fig. 1. Physical ladder-secondary DSLIM

There are two distinct approaches to estimate cogging forces: analytical and numerical ones. The analytical approaches are suitable for relatively simple geometry, but may cause inaccuracy due to simplification [9]. Nonetheless, analytical methods provide closed-form solutions that can offer insightful performance predictions with confidence, which make them ideally suited for preliminary design [10].

The magnetic flux path in the air gap of linear electrical motors is normally difficult to be estimated. The cogging force problem has been solved by recognizing the magnetic flux paths, because the magnetic flux path generates the flux density and magnetic energy in the air gap [11]. In cases of cogging forces, it will be related to leakage of magnetic flux path in the air gap. Some methods have been developed to predict the magnitude of cogging forces analytically. Using numerical approximation actually is already well conducted, however, this approximation cannot provide a closed form of mathematical expressions and is time-consuming [12].

As the first solution of cogging force prediction was the implementation of the first analytical approaches for the determination of cogging force value using leakage Zig-Zag permeance estimation [13]. The calculation was based on the magnetic potential in the air gap and relative position between teeth in the primary and secondary side which was called the "overlap method". However, the results of this method were not precise, because the fringing effect of corner magnetic circuit was neglected. But, this method was developed for rotary induction motors, so it cannot be applied to the linear induction motor [5].

For simplicity of pulsation force (cogging forces) calculation, on the other method, the air gap is assumed to be entirely smooth, with the conductors disposed at points on the surface. The aim of this method was reducing the cogging action problem to a one-dimensional one in some cases [14]. However, by neglecting the presence of slots, it cannot represent the real motors, because in the primary side and on secondary sides of electrical motors, there are large slots. Therefore, in this way, it is not possible to represent some of the components of leakage flux – cogging forces – in a satisfactory way [15].

The other simple way of determination of cogging forces was the integration of the lateral forces along the slot sides [16]. Due to its simplicity and reasonable accuracy, it was based on typical assumptions: cogging forces can be formulated as the net lateral force acting on the stator teeth, which can be achieved in three stages. First, the air gap flux density distribution of the ideal slotless machine is derived. Then, the simplified air gap reluctances responsible for slot opening effect are deduced to modify the air gap flux density. Finally, cogging forces are computed by synthesizing the force developed by each single slot. With the assumption of slotless machine, cogging forces in linear induction motors cannot be estimated exactly, because on the magnetic circuit of the linear motor for each side of the motor the air gap areas are connected to free air [17].

On the contrary, the numerical methods, which are normally implemented by two-dimensional (2-D) and three-dimensional (3-D) FEA methods, offer more accurate results for even complex geometry [18]. However, FEA methods are always computationally intensive, and will become extremely time-consuming for optimization involving numerous repetitive computations. FEA method should have the smallest meshing for getting precise results, however smaller meshing can lead to increasing time of the process [16].

Consequently, for designing linear induction motors with precise movement, an analytical method for determination of the magnitude of cogging forces is required. This can be done easily and produce precise results and not complicated calculation and short time-consuming. With equivalent between the magnetic circuit with the electrical circuit, there are possibilities to predict the flux density in the air gap easily. The variation of flux density in the air gap can affect cogging forces, so that using reluctance network equivalent, it is possible to have closed solution and short time-consuming.

3. The aim and objectives of the study

The aim of the research is the prediction of cogging forces on a ladder secondary double-sided linear induction motor, which will provide the closed solution and algorithm for designing a precision linear induction motor. To achieve the aim, the following objectives are set:

– to build one simple model of the magnetic circuit with the air gap area, which can generate an effective way for arranging reluctance network equivalent in a small model with the air gap;

– to investigate the effective air gap length with reluctance network equivalent, which can determine flux densities in the air gap area and the existence of magnetic energy variation;

– to perform a simulation of the multi-tooth model of the magnetic circuit with the air gap area, which allows investigating the trend of cogging forces in that model;

– to calculate cogging forces for the multi-tooth model which is employing the algorithm that has been developed in this research;

– to build a test-bed experiment of the multi-tooth model for measuring cogging forces with air gap length and current variation.

4. One-tooth model

The one-tooth model consists of two parts: moving part and stationary part. The current carrying coil is placed in the moving part. The distance between the movable and unmovable parts is separated by the air gap. Fig. 2 shows the simple one-tooth model. The moving part has only one slot and the stationary part has one right tooth that is smaller in width than the left one. Table 1 shows the geometrical dimensions of the model.

Table 1

Geometrical dimensions of the one-tooth model

No.	Moving part (mm)		Stationary part (mm)		
	slot	tooth	slot	left tooth	right tooth
1	15	10	15	40	10

Fig. 2 shows a moving core magnetized by the current-carrying coil. The one-tooth model is made from iron. If it is assumed that iron is unsaturated then the relative permeability of the iron is far higher than the air, so most of the magnetic flux will be confined to the iron. The flux Φ through any cross-section of the movable core will then be substantially similar.

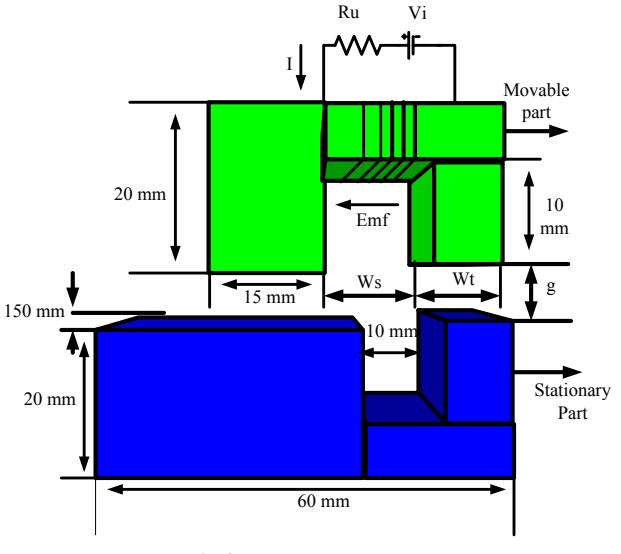

Fig. 2. Simple one-tooth model

In the analysis of the one-tooth model, two flux paths are considered: (1) flux passes straight across the air gap, without spreading into the surrounding air, (2) flux passes into the surrounding air (Fig. 3).

Fig. 4 shows the flux density distribution in the one-tooth model and resistance equivalent of the model. Each simplified flux path can be stated in the reluctance form of the air gap. For simplifying the magnetic circuit analysis, the electrical circuit equivalent can be approximated. This approximation is shown in Fig. 3 where it is assumed that the iron permeability is infinite, so the reluctance of iron materials $\Re_1, \Re_2, \Re_3$ will be much smaller and assumed negligible in the calculation. Fig. 4 can be used for flux density analysis in the air gap.

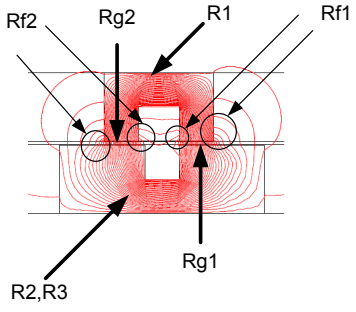

Fig. 3. Flux densities in the one-tooth model

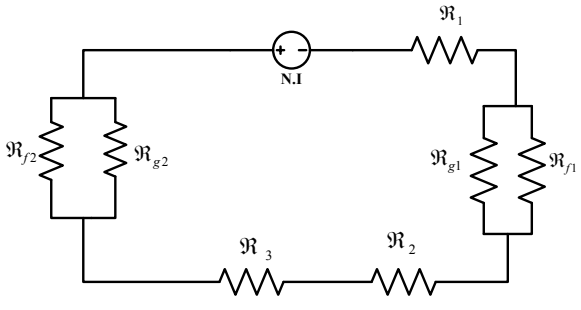

Fig. 4. Equivalent circuit of the one-tooth model

The value of magnetic reluctances is calculated based on the size of the slots in the moving part, the number of turns has been defined 45 turns (N) and maximum current which is flowing in the coil is 8.5 A (I), so the MMF=$N{\cdot}I$ is 382.5 At. The reluctance of all magnetic materials employs the equation:

$$\Re = \frac{L}{\mu_r \mu_0 A}, \tag{1}$$

where μ_r – relative permeability of used materials; μ_0 – permeability of air vacuum $\mu_0 = 4\pi(10^{-7})$ H/m; A – surface area.

Referred to Fig. 3 and general formula shown by equation 1 for obtaining a magnetic reluctances, hence:

$$\Re_1 = \frac{60 \cdot 10^{-3}}{4\pi \cdot 10^{-7} \cdot 3000 \cdot 10^{-5}} (\text{MA/Wb}). \tag{2}$$

The other reluctances are calculated by (2). The air gap reluctance can be calculated, for example in (3), the air gap length is 0.7 mm (L) and model depth is 1 mm, so the area of the right tooth is 10 mm^2, the result is shown by (3).

$$\Re_{g1} = \frac{0.7 \cdot 10^{-3}}{4\pi \cdot 10^{-7} \cdot 10^{-5}} = 55.00\,(\text{MA/Wb}). \tag{3}$$

The other reluctances are:

$$\Re_{g2} = \frac{0.7 \cdot 10^{-3}}{4\pi \cdot 10^{-7} \cdot 0} = \infty \text{ (open circuit)}, \tag{4}$$

$$\Re_{f1} = \frac{0.7 \cdot 10^{-3}}{4\pi \cdot 10^{-7} \cdot 10^{-5}} = 55.00\,(\text{MA/Wb}), \tag{5}$$

$$\Re_{g1} = \frac{10.7 \cdot 10^{-3}}{4\pi \cdot 10^{-7} \cdot 10^{-5}} = 851.9\,(\text{MA/Wb}), \tag{6}$$

$$\Re_2 = \frac{30 \cdot 10^{-3}}{4\pi \cdot 10^{-7} \cdot 3000 \cdot 10^{-5}} = 0.8\,(\text{MA/Wb}), \tag{7}$$

$$\Re_3 = \frac{20\cdot10^{-3}}{4\pi\cdot10^{-7}\cdot3000\cdot10^{-5}} = 0.53\,(\text{MA/Wb}), \quad (8)$$

$$\Re_{g1}//\Re_{f1} = \frac{\Re_{g1}\cdot\Re_{f1}}{\Re_{f1}+\Re_{g1}} = \frac{55.00\cdot851.9}{55.00+851.9} = 51.66\,(\text{MA/Wb}). \quad (9)$$

$$\Re_t = \Re_1 + \Re_2 + \Re_3 + 2(\Re_{g1}//\Re_{f1}) = 106.5\,(\text{MA/Wb}).$$

$$\Re_{g1}//\Re_{f1} = \frac{55.00\cdot851.9}{55.00+851.9} = 51.66\,(\text{MA/Wb}).$$

$$R_{g1}//R_{f1} = \frac{55.00\cdot851.9}{55.00+851.9} = 51.66\,(\text{MA/Wb}).$$

The magnetic flux in the air gap regions therefore is:

$$\varphi = \frac{N\cdot I}{\Re_t} = \frac{45\cdot8.5}{106.5} = \frac{382.5}{106.5} = 3.5\mu\text{ Wb}. \quad (10)$$

The flux density in the right side of the tooth is calculated with the right side area (A) of the tooth in 10 mm, so the result is shown by eq. (11).

$$B_{avg} = \frac{\varphi}{A} = \frac{3.5}{10} = 0.35\ \text{Tesla}, \quad (11)$$

where B_{avg} – the average normal flux densities on the air gap.

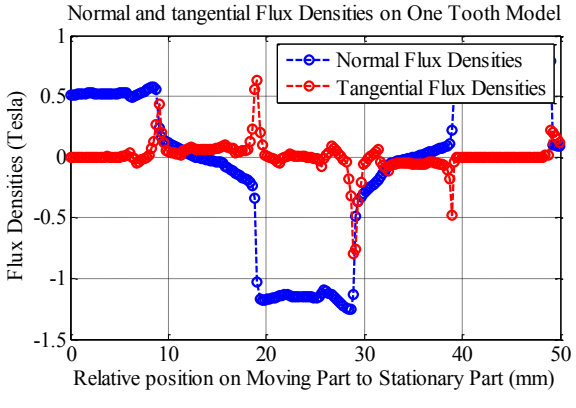

Fig. 5. Normal and tangential flux densities on the right side of the one tooth model

Compared with simulation results, 0.38 T, it has an error about 7 %. The simulation results have been shown in Fig. 5. For the left side of the model, the flux density is decreased to:

$$B_{left} = \frac{\varphi}{A_{left}} = \frac{3.5}{15} = 0.23\ \text{Tesla}, \quad (12)$$

where B_{left} – the average flux densities on the left air gap, A_{left} – the left region of model

Compared with FEM calculation is 0.24 Tesla, it has an error about 4 %. Fig. 6 shows simulation results for flux density distribution on the left side of the model.

$$\Re_{g1} = \frac{0.7\cdot10^{-3}}{4\pi\cdot10^{-7}\cdot0.9\cdot10^{-5}} = 62.00\ (\text{MA/Wb}), \quad (13)$$

$$\Re_{g2} = \frac{10.7\cdot10^{-3}}{4\pi\cdot10^{-7}\cdot0.1\cdot10^{-5}} = 852.0, \quad (14)$$

$$\Re_{g1}//\Re_{g2} = \frac{\Re_{g1}\cdot\Re_{g2}}{\Re_{g1}+\Re_{g2}} = \frac{62.0\cdot852.0}{(62.0+852.0)} = 57.8, \quad (15)$$

$$\Re_{g4} = \frac{10.7\cdot10^{-3}}{4\pi\cdot10^{-7}\cdot1.1\cdot10^{-5}} = 774.4\ (\text{MA/WB}), \quad (16)$$

$$\Re_{g3}//\Re_{g4} = \frac{\Re_{g3}\cdot\Re_{g4}}{\Re_{g3}+\Re_{g4}} = \frac{55.0\cdot774.4}{55.0+774.4} = 51.32, \quad (17)$$

$$\varphi = \frac{N\cdot I}{\Re_T} = \frac{382.5}{112.4} = 3.41\mu\text{ Wb}, \quad (18)$$

$$B_{\max} = \frac{\varphi}{A} = 0.38\ \text{Tesla}, \quad (19)$$

$$B_{left} = \frac{\varphi}{A_{left}} = 0.21\ \text{Tesla}. \quad (20)$$

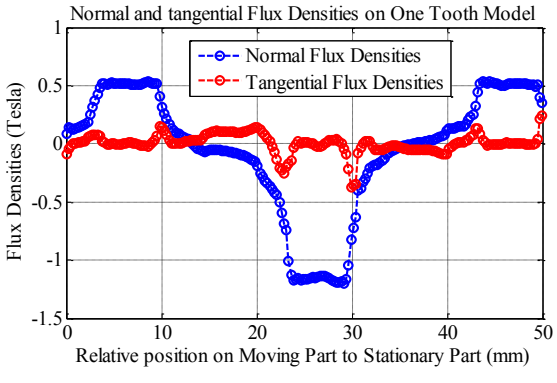

Fig. 6. Normal and tangential flux densities on the left side of the one tooth model

For position – 3 mm, the upper part will be moved to the left direction for about 2 mm length.

$$\Re_{g1} = \frac{0.7\cdot10^{-3}}{4\pi\cdot10^{-7}\cdot0.8\cdot10^{-5}} = 69.7\ (\text{MA/Wb}), \quad (21)$$

$$\Re_{g2} = \frac{10.7\cdot10^{-3}}{4\pi\cdot10^{-7}\cdot0.2\cdot10^{-5}} = 425\ (\text{MA/Wb}), \quad (22)$$

$$\Re_{g1}//\Re_{g2} = \frac{\Re_{g1}\cdot\Re_{g2}}{\Re_{g1}+\Re_{g2}} = \frac{62\cdot852}{62+852} = 57.8\,(\text{MA/Wb}). \quad (23)$$

The average flux density for one slot pitch using the Green approximation can be calculated by determining the reluctance for one slot pitch based on the fringing coefficient on the Green curves. Table 2 shows the comparison between Green approximation and reluctance network equivalent method. The fringing flux will be bigger, if the air gap length is enlarged. It is caused that the permeability of the air gap is very small, so reluctances are bigger and the fringing flux also is bigger. Based on the whole data in Table 2, the RNE approximations are close to the FEM results.

Table 2

Comparison for the model with 10 mm slot

g	Average flux density			Error	
(mm)	(Tesla)			(%)	
	FEM	Green	RNE	Green	RNE
1	0.47	0.58	0.47	23.56	0.12
1.1	0.43	0.54	0.44	24.32	1.01
1.2	0.4	0.5	0.4	23.36	0.41
1.3	0.38	0.47	0.37	24.61	1.87
1.4	0.35	0.42	0.35	19.42	1.33
1.5	0.33	0.39	0.32	18.46	2.28
1.6	0.31	0.37	0.3	18.37	3.1
1.7	0.3	0.35	0.29	18.16	3.82
1.8	0.28	0.34	0.27	18.95	4.48
1.9	0.27	0.33	0.26	19.73	5.05
2	0.26	0.32	0.25	22	5.36

6. Effective air gap length (EAGL)

The cogging force estimation requires the knowledge of the flux density in the air gap. The air gap length does not remain constant as the motor moves. Therefore, the approximation of the effective air gap length (EAGL) will be determined for obtaining the cogging force prediction.

The approximation of the EAGL can be obtained based on the flux density distribution in the air gap. The flux density distribution in the air gap in relation to the magnet-motive force (MMF) is a non-linear problem. The magnetic circuit contains iron in which the relationship between the intensity of magnetic flux and the magnet-motive force is a non-linear magnetic circuit problem, therefore, it can be often solved by graphical approximation which can describe the relationship between the flux and magnet-motive force in magnetization curves.

This section derives approximations for flux paths of both models. This section focuses on the RNE method in which the flux path. Fig. 5 shows the approximations used for flux paths in the model. The magnetic flux lines between the teeth are straight lines perpendicular to the iron surfaces, while the fringing flux is approximated by circular shapes as shown in Fig. 5. This model consists of two slot pitches: right and left slot pitch. It is caused that the tooth width on the left side is different from the tooth width on the right side. The slot pitch of the left side is α and right side is β.

Assuming infinitive permeability of the core, the permeance of flux paths can be determined by the equation:

$$P = \upsilon \frac{S}{L} [4], \tag{24}$$

where μ – the permeability of material; S – two cross sections of the opposite tooth in square meter (Fig. 7); L – distance between the opposite teeth (Fig. 7).

$$P_2 = \mu_0 \frac{\omega_{tr} \cdot d_p}{g} = \frac{\omega_{tr} \cdot d_p}{g}, \tag{25}$$

where μ_0 – air permeability (equal to 1); ω_{tr} – right tooth width; d_p – Yoke depth; g – actual air-gap length.

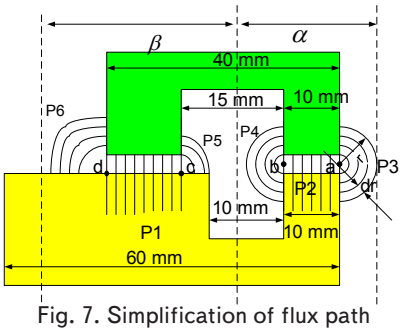

Fig. 7. Simplification of flux path

For the conductance in the right tooth, straight lines of flux path have the conductance P_3 and P_4:

$$dP_3 = dP_4 = \frac{dr \cdot d_p}{g + (\pi \cdot r)}, \tag{26}$$

where dr – small difference of circular shape; r – radius of circular flux magnetic shape (max until half of the slot pitch). Then:

$$P_3 = P_4 = \int_0^{(\omega_s/4 - x)} \frac{d_p}{\pi \left(\frac{g}{\pi + r} \right)} \mathrm{d}r =$$

$$= \frac{d_p}{\pi} \int_0^{\left(\frac{\omega_s}{4-x}\right)} \frac{dr}{\left(\frac{g}{\pi + r} \right)} = \frac{d_p}{\pi} \left[\ln \left(\frac{g}{\pi} + r \right) \right]_0^{(\omega_2/4 - x)},$$

so

$$P_3 = P_4 = \frac{d_p}{\pi} \ln \left(\left(\frac{g}{\pi} + \left(\frac{\omega_s}{4} - x \right) \right) / \frac{g}{\pi} \right) =$$

$$= \frac{d_p}{\pi} \ln \left(1 + \left(\frac{\omega_s}{4} - x \right) \frac{\pi}{g} \right) = \frac{d_p}{\pi} \ln \left(\frac{g + (\omega_s - x) \frac{\pi}{4}}{g} \right). \tag{27}$$

Therefore, the total conductance over one slot pitch is:

$$P_{Right}(x = 0) = \frac{P_2 + P_3 + P_4}{\omega_\tau} =$$

$$= \frac{\frac{\omega_{tr} \cdot d_p}{g} + 2 \frac{d_p}{\pi} \ln \left(1 + \frac{(\omega_s - x)\pi}{4g} \right)}{\omega_\tau}. \tag{28}$$

The reciprocal of this conductance (magnetic conductance) quantity is the reluctance of magnetic flux ($\Re$) of the air-gap cross section for an average length when the x variable is equal to zero (x=0). The position x of zero value means that the middle of the tooth on the moving part of the model exactly coincides with the middle of the tooth on the stationary part. The reluctance of magnetic flux in the air gap for this simple model can be formulated as:

$$\Re \approx \frac{\alpha}{\frac{\omega_t \cdot d_p}{g} + 2 \frac{d_p}{\pi} \ln \left(1 + \frac{\omega_s \pi}{2g} \right)}. \tag{29}$$

Based on the relationship between reluctance and equivalent air-gap length per 1 mm length of the tooth width, $\Re = \frac{g_e}{d_p}$, so:

$$g_e \approx \frac{\alpha}{\frac{\omega_t}{g}+\frac{2}{\pi}\ln\left(1+\omega_s\pi/2g\right)} \approx \frac{\omega_t+\omega_s}{\frac{\omega_t}{g}+\frac{2}{\pi}\ln\left(1+\frac{\omega_s\pi}{2g}\right)}. \quad (30)$$

7. Multi-tooth model

The investigation of the flux density in this multi-tooth model aims to find the relationship between MMF (magneto-motive force) to the flux densities in the air gap of LIM. The moving part is designed with five teeth and four slotted areas in which the coil is placed. The number of teeth in the moving part and in the stationary part is different. The stationary part has 7 teeth and 8 slots. The materials of both parts are made from iron. Fig. 8 shows the multi-tooth model.

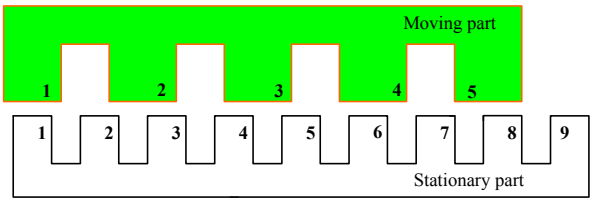

Fig. 8. Multi-tooth model

With the constant ampere-turns and constant ratio of the slot and tooth width of the movable part, and variation of the air gap length from 1 to 2 mm with steps of 0.1 mm, the cogging forces will be calculated using the overlap method. The fringing effect will be taken into account.

The arrangement of coils in slots of the multi-tooth model is shown in Fig. 9. The current-carrying coils are placed as shown with current directions also shown. This arrangement based on the phase difference between slots should be 120°. Table 3 shows the geometrical dimensions of the multi-tooth model.

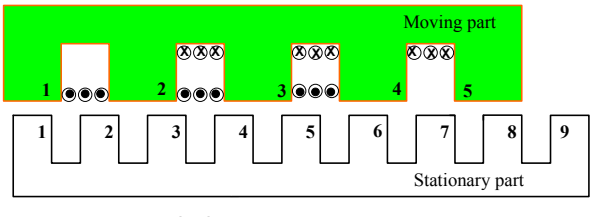

Fig. 9. Coils arrangement in slots

Table 3

Dimensions of the multi-tooth model

No.	Slot width		Tooth width	
	Moving	Stationary	Moving	Stationary
unit	(mm)	(mm)	(mm)	(mm)
1	15	10	10	10

8. Cogging forces calculation on the multi-tooth model

Analysis of cogging forces is conducted for the moving part of the multi-tooth model which is moving through one slot pitch. The first condition is where the tooth of the moving part is directly opposite to the stationary part tooth. Secondly, the tooth on the moving part is partly opposite to the stationary tooth and partly opposite to the stationary slot; and the third is where the moving part tooth is directly opposite to the slot.

Using the Cedrat-FLUX software, the multi-tooth model is simulated (Fig. 10). The simulation of the cogging forces appearing at very low speed or even at standstill. The electrical current flowing in the coils of the moving part is 5 amperes. In this simulation, the cogging force at each tooth is measured and shows that cogging on the end of the model can cancel each other.

The distribution of flux density in the air gap can be determined by taking account of fringing effects. Based on the flux density, the magnetic energy variation can be calculated and then the possibility of obtaining the cogging forces analysis in the air-gap can be obtained.

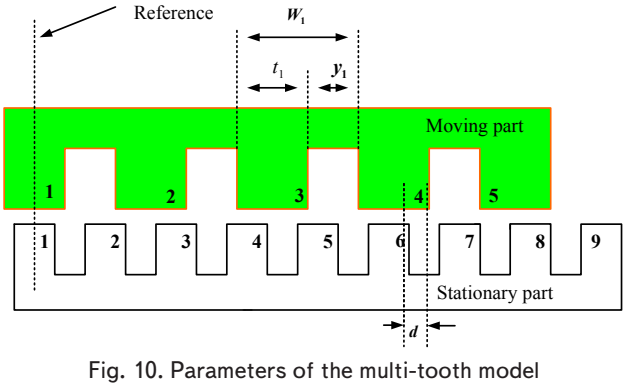

Fig. 10. Parameters of the multi-tooth model

$$MMF_{drop} = 4\pi n_1 i_1 \frac{d}{W_1}, \quad (31)$$

where MMF_{drp} – magnetic motion force in the air gap; n_1 – number of coils in the moving part; i_1 – electrical current flowing into the coil; d – distance between the teeth on moving and stationary parts; W_1 – distance between the teeth in moving parts.

The overlap method can be used as the moving part moves slowly. The tooth of the moving part meets with the tooth and the slot of the stationary part. The variation of relative position between the tooth and the slot on each part is divided into three conditions: (a) the moving part is entirely opposite to the stationary part teeth (Fig. 11); (b) the moving part is partly opposite to the stationary part tooth and partly opposite to the stationary part slot (Fig. 12).

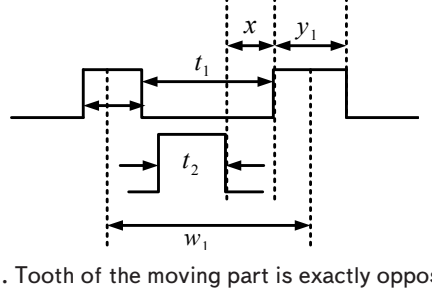

Fig. 11. Tooth of the moving part is exactly opposite to the tooth of the stationary part

The cogging force can be calculated by first deriving an expression of magnetic energy stored in the air gap as a function of the relative position of the tooth of the moving part to

the tooth of the stationary part. Cogging forces can be calculated by differentiating the energy expression. The magnetic energy stored in the air gap between teeth can be described as the multiplication between the magnetic potential of the pair of teeth and the conductance of the magnetic flux path.

$$W = \frac{V_T^2 P}{8\pi}, \tag{32}$$

where V_T – magnetic potential difference between two teeth; P – conductance of the flux magnetic path. The first step of the calculation is deriving the magnetic energy stored in the air gap in each region. The total magnetic energy can be obtained by the addition of the energy in every region.

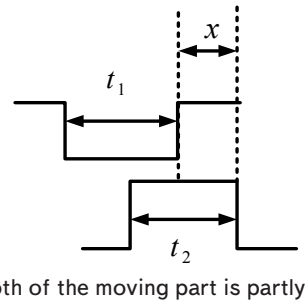

Fig. 12. Tooth of the moving part is partly opposite to the tooth of the stationary part

8. 1. First condition

The magnetic field storage can be represented by the magnetic equation below. This condition begins from the middle of the tooth of the moving part, coincides exactly to the middle of the stationary part tooth, and continues to the point where the secondary tooth has traveled until its left edge lines up with the left edge of the primary tooth.

$$W_{fa} = Qt_p x^2, \quad 0 < x < \frac{t_s - t_p}{2}, \tag{33}$$

where Q is a constant. The Q constant will be derived in the previous section. The cogging force can be obtained by deriving equation 33 with respect to displacement x:

$$F_{fa} = \frac{dW_{fa}}{dx} = 2Qt_p x, \quad 0 < x < \frac{t_s - t_p}{2}. \tag{34}$$

8. 2. Second condition

The magnetic energy stored in the air gap for this condition is:

$$W_{fb} = Qx^2\left(\frac{t_p + t_s}{2} - x\right), \quad \frac{t_s - t_p}{2} < x < S_p - \frac{t_s - t_p}{2}. \tag{35}$$

The derivative of the equation 28 will provide the cogging force for this region:

$$F_{fb} = \frac{dW_{fb}}{dx} = 2Qx\left(\frac{t_p + t_s}{2} - x\right) - Qx^2, \quad 0 < x < S_p. \tag{36}$$

8. 3. Third Condition

In this condition, the energy is affected by two directions of flux paths, one due to the flux from the left moving part tooth and the other due to the flux from the next tooth on the right.

$$W_{fc} = Qx^2\left(\frac{t_p + t_s}{2} - x\right) + Q\left(w_{\tau p} - x\right)^2\left(x - S_p + \frac{t_s - t_p}{2}\right),$$

$$S_p - \frac{t_s - t_p}{2} < x < \frac{\omega_{\tau p}}{2}; \tag{37}$$

$$F_{fc} = \frac{dW_{fc}}{dx} = Q\left(w_{\tau_p} - 2x\right)\left(2w_{\tau p} + S_p - t_s\right). \tag{38}$$

For the analysis of cogging forces, the three equations will be substituted with the dimensions of the model: g (air-gap)=1.5 mm; (secondary slot width) S_S=15 mm; (secondary tooth width) t_s=13 mm; (moving part width) t_p=15 mm; (moving part slot width) S_p=15 mm; (end tooth width) W_{end}=20 mm; (depth of the primary layer) L=75 mm. The cogging forces for every condition are:

F_{fa}=0.8·Q·x for 0<x<0.065;

F_{fb}=Q·x(0.930–3x) for 0.065<x<0.335;

F_{fc}=2.94Q(0.400–x) for 0.335<x<0.400.

8. 4. Q parameter calculations

The current flowing in the coils with a specific number of turns at the slots of the moving part generates the distributed flux magnetic field in the air gap. The relationship between ampere-turn of the coil and flux magnetic field can be described in the following equation

$$\varphi = BA = \frac{4\pi\mu A \cdot N \cdot i \cdot 10^{-7}}{g} \text{ (Webers)}, \tag{39}$$

where φ – magnetic flux; A– area cross section; B – magnetic flux distribution; N – turn number of the coil; i – current flowing into the coils; g – air gap length.

If the voltage is impressed in the coil suddenly, the voltage induced in the circuit, opposing the impressed voltage:

$$e = -N\frac{d\varphi}{dt} = -\frac{4\pi\mu N^2 A.10^{-7}}{g}. \tag{40}$$

Then the amount of energy delivered to the magnetic field during the time t:

$$W_f = -\int_0^t e \cdot i \cdot \mathrm{d}t =$$

$$= \frac{4\pi\mu N^2 A \cdot 10^{-7}}{g}\int_0^i i\mathrm{d}i = \frac{2\pi\mu N^2 A \cdot 10^{-7} i^2}{g}, \tag{41}$$

$$W_f = \frac{B^2 A g}{8\pi\mu} \text{ (Joules)},$$

$$W_f = \frac{B^2 \cdot A \cdot g \cdot 10^7}{8\pi \cdot \mu} = \frac{V^2 P}{8\pi} \text{ (Joules)}, \tag{42}$$

where V – magnetic potential in the air gap; P – conductance of the flux magnetic path; W_f – magnetic energy stored in the air gap.

Based on the variation of the above magnetic energy equation, the cogging forces can be calculated by using the reluctance circuits equivalent method. Based on the relationship between flux density in the air gap and MMF:

$$B=\frac{4\pi\cdot NI_{rms}}{g\cdot 10^{7}}\ (\mathrm{Wb/m^2}), \tag{43}$$

where B is the average of the flux density in the air gap. Without taking into account the fringing effect in each tooth, as the moving part moves, the flux density distribution is changed and depends on the relative position of the moving part to the reference point. The reference point is defined when one of the middle of the tooth of the moving part coincides with the middle of the tooth in the stationary part. The calculation of B as a function of the relative position (x) can be obtained using:

$$B(x)=\frac{1.26\cdot N\cdot I_{rms}}{g\cdot 10^{8}}\left(\frac{x}{w_p}\right)(\mathrm{W_b/m^2}), \tag{44}$$

where I_{rms} – rms current in one primary slot; g – air gap length; w_p – primary slot pitch.

If the above flux density equation is substituted into the stored energy equation in the air gap, then:

$$W_f=\frac{B^2\cdot A\cdot g\cdot 10^{7}}{8\pi\mu}=$$
$$=\frac{\left(\frac{1.26\cdot N\cdot I_{rms}}{g\cdot 10^{8}}\left(\frac{x}{w_p}\right)\right)^2 10^{7}\cdot g\cdot t_p\cdot D_p}{8\pi}(\mathrm{Joules}). \tag{45}$$

The energy per slot pitch therefore is:

$$W_f=\frac{0.632}{10^{8}}\frac{N^2I_{rms}^2D_p}{gw_p^2}(x^2t_p)(\mathrm{Joules/tooth}), \tag{46}$$

where N – the number of turns in the primary part; I_{rms} – rms-value of the current in each conductor of the coil; D_p – depth of the primary part; g – air gap length; t_p – tooth width of the primary part; x – relative position of the primary part to the secondary part.

The cogging forces will be calculated by using the stored energy magnetic variation in the air gap, so it can be obtained by differentiating the magnetic energy equation to give:

$$F_{cg}=\frac{1.264}{10^{8}}\left(\frac{N^2I_{rms}^2\cdot D_p}{g\cdot w_p^2}\right)(x\cdot t_p)(\mathrm{Newton}). \tag{47}$$

The Q parameter can be obtained by substitution of the above equation into the equation:

$$F_{cg}=2\cdot Q\cdot t_p\cdot x=\frac{1.264}{10^{8}}\left(\frac{N^2I_{rms}^2\cdot D_p}{g\cdot w_p^2}\right)\left(x\cdot t_p\right). \tag{48}$$

Then the Q parameter is:

$$Q=\frac{0.632}{10^{8}}\left(\frac{N^2I_{rms}^2\cdot D_p}{g\cdot w_p^2}\right). \tag{49}$$

This equation (41) is used for cogging force calculation with inserting the Q parameter for the first condition and the other condition can employ equations (34), (34) and (35).

9. FEM analysis results

Fig. 13 shows the designed multi-tooth model on 2D Cedrat-software. The winding structures of the moving part haven't been defined in this model. The red color area represents the moving part teeth area, and pink color is stationary teeth. Green color shows slots of the stationary part.

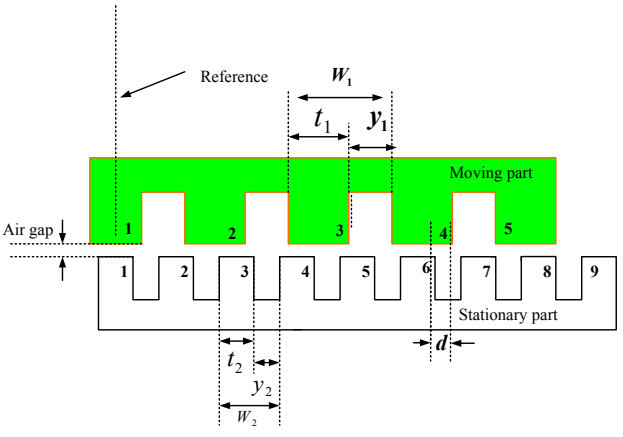

Fig. 13. Dimensions of the multi-tooth model

In this simulation, the cogging force at each tooth is measured and shows that cogging on the end of the model have a similar form, so the cogging forces are dominated by cogging forces in the middle areas. Fig. 14 shows the difference of cogging forces at each tooth of the moving part. At tooth 1, the curve shows that electromagnetic forces always have a positive value and never go to a negative value. It is caused that in the end area of the linear induction motor, there is some magnetic leakage in which the electromagnetic forces between the tooth in the moving and in the stationary part can be reduced. On the opposite tooth, tooth 5 shows that the signal electromagnetic forces always have a negative value. Both signals cancel each other.

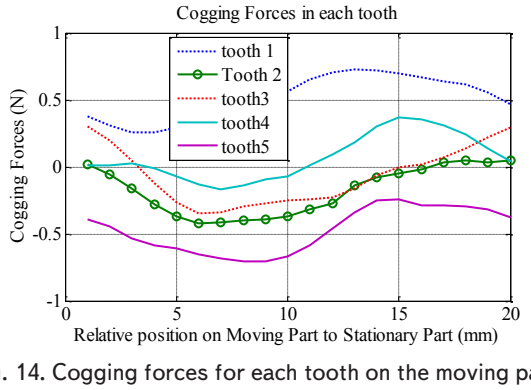

Fig. 14. Cogging forces for each tooth on the moving part

Fig. 15 shows the total of cogging forces in the three-model simulation. This simulation aims at evaluating the results. In this case, the curve shown by Fig. 15 the force in the simulation is cogging force. It is related to cogging forces characteristic that the cogging force signals should be provided as periodic signals in which its wavelength is similar to the pole pitch of the linear induction motor.

From Fig. 15, it can be concluded that the electromagnetic force in the air gap area of the linear induction motor is cogging forces while the moving part moves slowly. Even though the signal on tooth 1 and 5 is not periodic (Fig. 14), but if the electromagnetic forces on all teeth are added, the signal is periodic and has a period time similar to the pole pitch of the linear induction motor. Be referred in Table 3 that the slot and tooth width of the moving part is 25 mm, so

the pole pitch of the model is 25 mm. As shown in Fig. 15, the signal fluctuates after 25 mm, so that the electromagnetic forces can be classified as cogging forces. The maximum of cogging forces is 25 N.

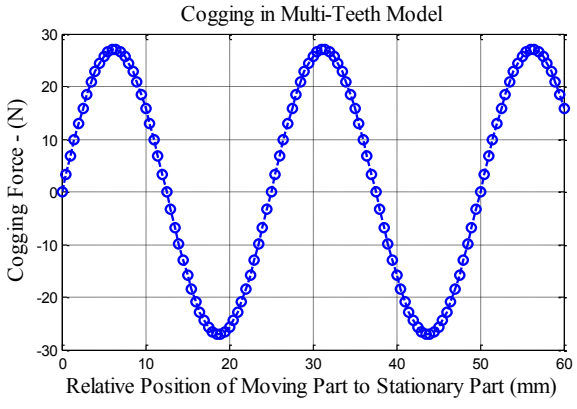

Fig. 15. Total cogging forces of the multi-tooth model

10. Discussion of the relationship between magnetic energy and cogging forces

This section will describe (1) the comparison results between the analytical and FEA results of cogging forces calculations for the one-tooth model. The model will be referred to as the simple model, including only one coil. It consists of stationary and moving parts in which the excitation coil is placed. The reference directions of coil current and flux linkage are also described. The resistance R in series connected to the source aimed to limit the current in steady state with the assumption that the voltage of the source is constant.

The excitation coil is placed in the moving part as resemble to kind of the linear induction motor construction with the short primary layer. Compared with FEM results, the analytical calculation result is 0.24 Tesla, so it has an error about 4 % in comparing with the FEM. The cogging forces in the air gap of the simple model can be determined. Fig. 16 shows the relationship between cogging forces and magnetic energy in the air gap. It can be seen that the gradient of energy with respect to the relative position between the upper member and bottom member describes the variation of cogging forces. When the moving part exists in relative position to the stationary part in between –5 mm; 0; +5, according to the Maxwell rule that the curve of magnetic energy can be obtained by the gradient of magnetic energy. In this range, the gradient of magnetic energy is in negative values. In relation to cogging forces, it means that cogging forces in between –5 mm to 5 mm have a negative value (Fig. 16) which the cogging forces can be calculated by the derivative of magnetic energy in the air gap.

10. 1. Discussion of cogging forces prediction on the one-tooth model

At the relative position 5 mm, the cogging forces come into zero value, in the energy curve, it is shown by zero gradient. It is caused that the leakage magnetic energy in the right and left tooth is similar, so totally the cogging force is zero. The magnetic energy before relative position 5 mm describes decreasing of energy which has a negative gradient, so the cogging force has a negative value (Fig. 16). However, after 5 mm, magnetic energy shows the increasing value, so the gradient of energy becomes positive and the cogging forces will be positive (Fig. 15).

Fig. 17 describes the comparison value of cogging forces between analytical results with the simulation result using FEA. In this case, the fringing effect was not taken into account. So that the curves on the max-min area, the values of cogging forces between the experimental and analytical results have some big error. In this area, the error is much bigger compared with the other area of curves. It is caused by while the moving part of the motor moves, the magnetic reluctance should be changed (according to the Faraday's law). If the leakage of magnetic flux is neglected, so that the precision level of calculation is decreased.

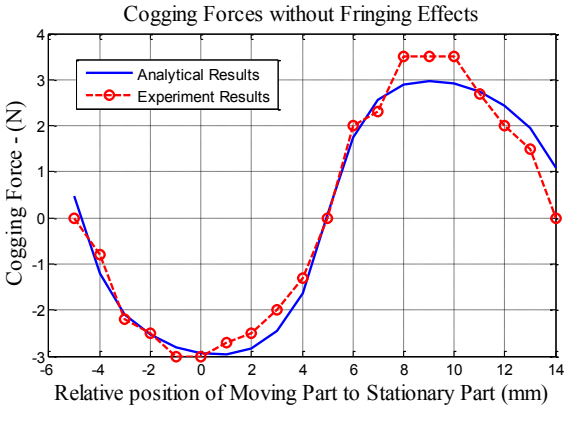

Fig. 17. Comparison between analytical and experiment results

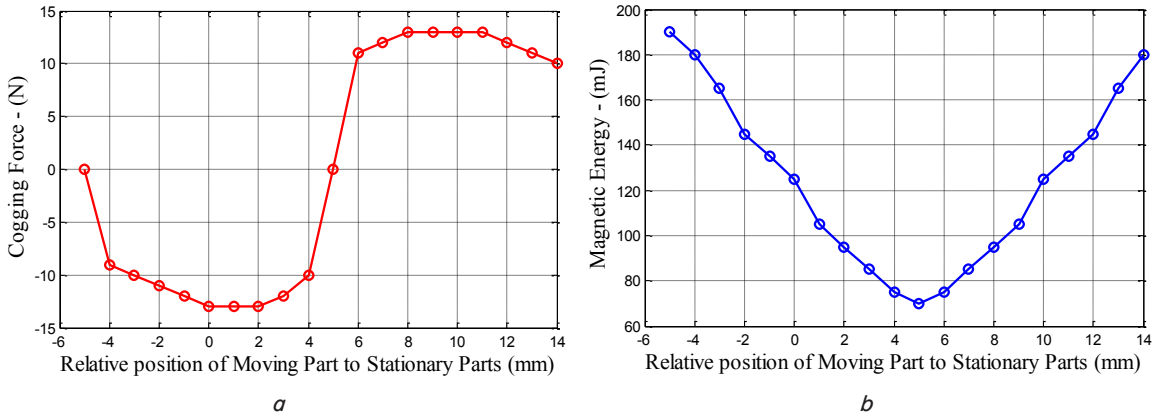

a *b*

Fig. 16. Simulation results: *a* – cogging forces; *b* – magnetic energy

Fig. 18 shows the trend of the analytical and experimental results with the fringing effect taken into account. According to the last calculation, the fringing effect based on Reluctance Network Equivalent (RNE) approximation supported by magnetic path estimation provided the improvement of calculation results. The improvement of the results could be perfectly done by using this approximation. The fringing coefficient was based on this method in which the calculation flux scattering was taken into account and the effective air gap length was also used in the cogging forces equations. The trend of analytical and experimental results provides results that the estimation method can predict the cogging force of LIM in precise results.

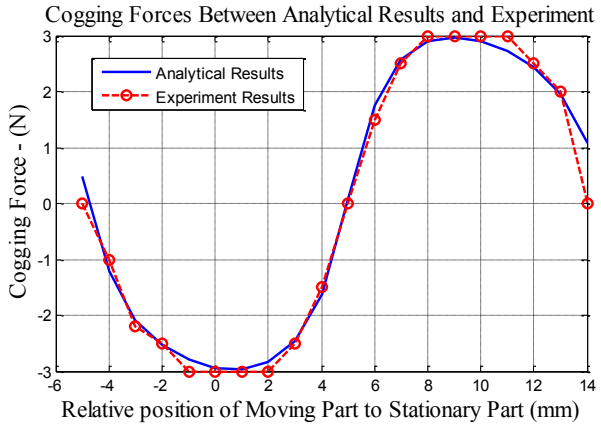

Fig. 18. Analytical and experimental results without fringing effects

10. 2. Cogging forces experiments on multi-tooth model

The multi-tooth model shown in Fig. 19 was developed for the purpose of experimental verification. The cogging force variation has been experimentally measured and the complete comparison with the predicted results is presented. Fig. 19 shows a diagram of the experimental test bed. Each coil is supplied by different DC signals to generate three-phase AC signals. The stationary part is connected to the load for measurement of cogging forces.

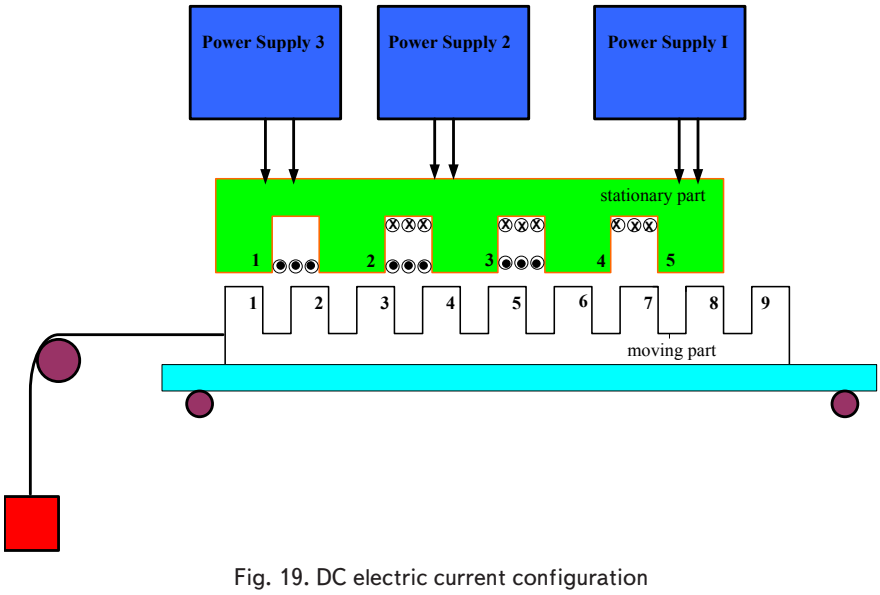

Fig. 19. DC electric current configuration

The test bed consisted of a moving part holder, a moving part, coils and a stationary part. The coils are connected to the DC-power supply. In the left side, the moving part is connected to loads. Fig. 20 shows the picture of the test bed of the multi-tooth model experiment. The force was measured by Digital Force Gauge with specifications: capacities from 0.5 to 500 lbf/2.5 to 2,500 N; USB, RS-232 and analog communication; normal and peak operating modes; integral or remote load cell; accuracy ±0.1 % of full scale. For each position, the force measurements have been done 10 times for one moving and 10 times for the opposite way. From the measurement, the measurement deviation was not more than 1 %.

Fig. 20. Picture of experimental test bed

Fig. 20 shows the physical experiment of the multi-tooth model. That model consists of two parts: moving part and stationary part. In this experiment, the moving part is uncoiled slot part. The coils are placed on the slots of the stationary part. The winding is arranged in double coils for middle slots and single slot on both ends of regions. The moving part consists of 8 slots and the stationary part is 4 slots. It means that the number of slots in the moving part was doubled to the number of slots in the stationary part. With this slots configuration, the experiment can measure the cogging forces for two periods.

10. 3. Discussion of experimental results of cogging forces for the air gap length and electrical current variation

This experiment was conducted to investigate the effects of air gap length variation and electrical current flowing into coils to electromagnetic forces in the air gap of the model. The air gap length will be varied between 0.55 mm and 1 mm. The coils were supplied by DC current 3 amperes and 4 amperes. The trends between the experimental and analytical results were plotted in the one graph, so the trend difference can be known properly.

Fig. 21 shows the graph trends between analytical results and experimental measurements. The results show that the model in RNE approxi-

mation provides similar trends with the experimental results. The experiment has been done for only one slot pitch movement since the cogging force is periodic. Fig. 21 shows experiments with air gap lengths of 0.55 mm. The measurement results show that the analytical model that is simulated using the m-program of MATLAB software-packages has a similar trend to experimental results. So the simulation justified the analytical results. As shown in the middle area, the fluctuation of measurement results was wider than in the other area, it is caused that in this area, the leakage magnetic paths are classified as extreme paths. Therefore, the electromagnetic forces cannot be measured precisely and also is caused by the magnetic paths on this area cannot be approximated by a certain shape.

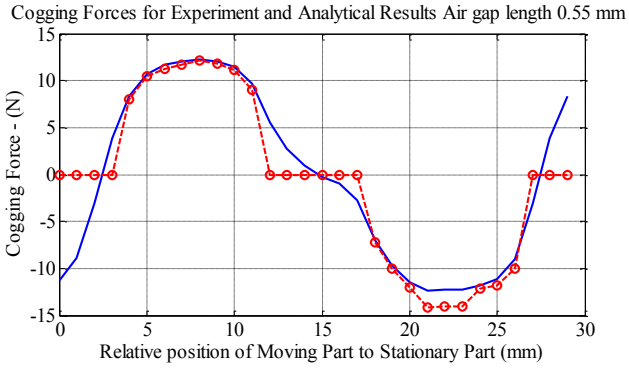

Fig. 21. Cogging forces measurement and analytical results with the air gap length 0.55 mm and current 4 A

Fig. 22 shows that the cogging forces in the middle region in which the experiment magnitude of cogging forces fluctuation are bigger than in the other regions. It is caused by the existence of leakage magnetic reluctance which is affected slotted area is wider than as the tooth in the moving and in the stationary meet exactly in a similar position. The magnitude of cogging forces with the smaller air gap length is bigger, it is affected by the electromagnetic forces proportional to the distance between the tooth in the moving part within the stationary parts.

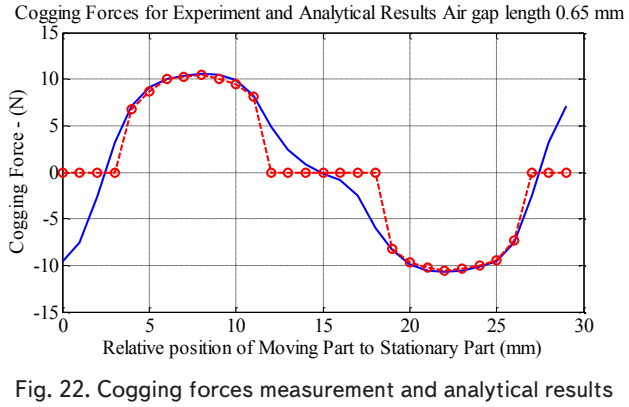

Fig. 22. Cogging forces measurement and analytical results with the air gap length 0.65 mm and current 4A

Fig. 23 shows similar phenomena with the previous figure. It shows that analytical results can represent the cogging forces in which the magnitude of cogging forces will be bigger if the air gap length is wider. The magnitude of cogging forces for 0.65 mm air gap length is about 22.5 N. It is caused according to the Maxwell stress rule that the smaller distance between the teeth in the moving and stationary part will affect bigger of electromagnetic forces.

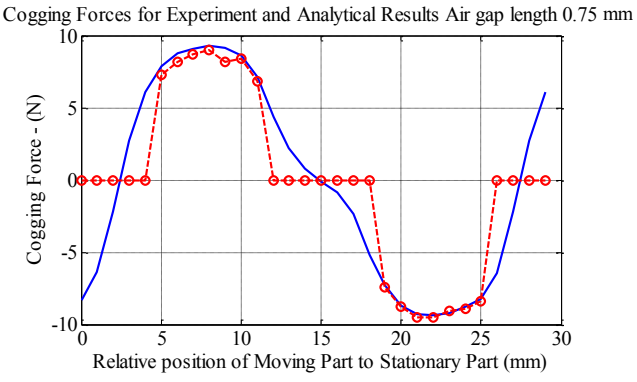

Fig. 23. Cogging forces measurement and analytical results with the air gap length 0.75 mm and current 4 A

Fig. 24, 25 have similar results in which the magnitude of cogging forces will be smaller if the air gap length is wider than in the previous model. The error of cogging measurement in the extreme area is bigger than in the other regions, because the existence of leakage magnetic fields in the slotted area can affect the analytical results of cogging forces predictions. Those are caused by the analytical equation has been rejected in this extreme area. So that the error between measurement and analytical results cannot be estimated very well for the extreme value of cogging forces.

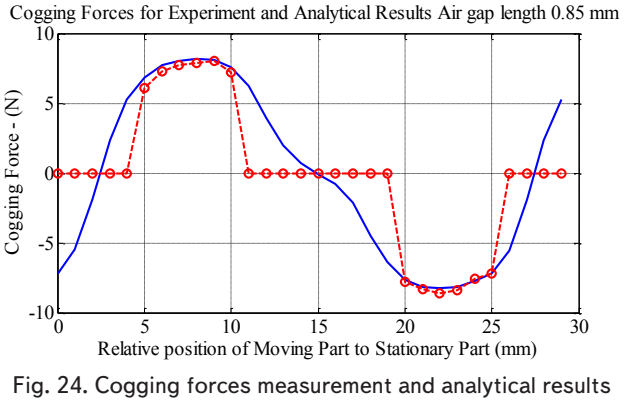

Fig. 24. Cogging forces measurement and analytical results with the air gap length 0.85 mm and current 4 A

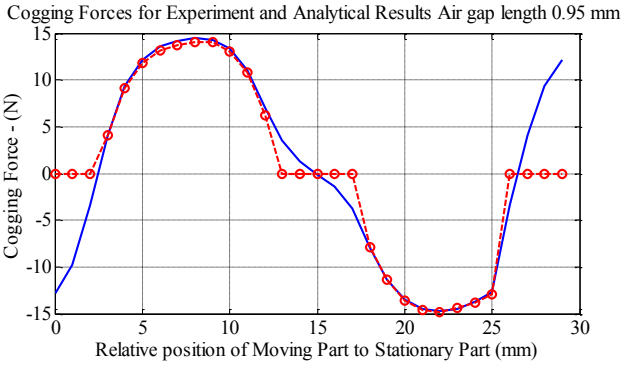

Fig. 25. Cogging forces measurement and analytical results with the air gap length 0.95 mm and current 4 A

The magnitude of cogging forces directly depends on the magnitude of current sources. The reason is that the electromagnetic forces which can generate cogging forces, between the core in the moving part and the iron core in the stationary part are affected directly by the magnitude of electric

current sources which flow into the coils in the moving part. Fig. 26 shows that the magnitude of cogging forces is smaller than the magnitude of cogging forces in Fig. 23. However, the shapes of both curves of cogging forces are similar. It means that the cogging forces in the extreme regions are different from the analytical results. The disadvantage of this method was that in the extreme area, the magnetic path shape cannot be approximated exactly, so the trend of the analytical results was not close to the measurement data.

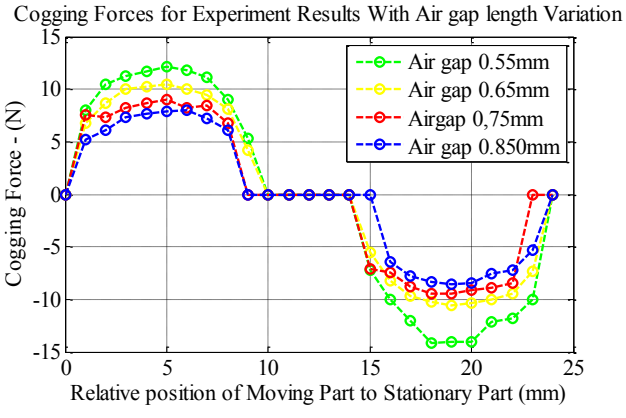

Fig. 26. Cogging forces measurement results with the air gap length variation and current 3 A

11. Conclusions

1. By introducing a reluctance network equivalent, the small one-tooth magnetic model can be analyzed precisely and easily. The flux densities in the air gap of the model can be found with a good result and compared with FEM result is about under 10 %.

2. The effective air gap length can be defined using the reluctance network circuits. It has been proved using the one-tooth model. Validation of the results is that it is for calculating the average flux densities in the one-tooth model. The comparison shows that the trend between the calculation results using EAGL and finite element method is small.

3. After meshing of the multi-tooth model, cogging force evaluation has been done and compared with the analytical results, which shows that the maximum difference between the analytical and simulation average results was under 5 %.

4. Cogging forces have been calculated on the multi-tooth model, and provide the value trend which is close to the experimental results that the maximum difference was about under 10 %.

5. The test bed experiment has been supported by the current generator and current measurement devices and force measurement digital device.

References

1. Calculation of cogging force in a novel slotted linear tubular brushless permanent magnet motor / Zhu Z. Q., Hor P. J., Howe D., Rees-Jones J. // IEEE Transactions on Magnetics. 1997. Vol. 33, Issue 5. P. 4098–4100. doi: https://doi.org/10.1109/20.619675
2. Prediction of cogging torque using the flux-MMF diagram technique / Deodhar R. P., Staton D. A., Jahns T. M., Miller T. J. E. // IEEE Transactions on Industry Applications. 1996. Vol. 32, Issue 3. P. 569–576. doi: https://doi.org/10.1109/28.502168
3. Various design techniques to reduce cogging torque by controlling energy variation in permanent magnet motors / Hwang S.-M., Eom J.-B., Jung Y.-H., Lee D.-W., Kang B.-S. // IEEE Transactions on Magnetics. 2001. Vol. 37, Issue 4. P. 2806–2809. doi: https://doi.org/10.1109/20.951313
4. Bianchi N., Bolognani S., Cappello A. D. F. Reduction of cogging force in PM linear motors by pole-shifting // IEE Proceedings – Electric Power Applications. 2005. Vol. 152, Issue 3. P. 703. doi: https://doi.org/10.1049/ip-epa:20045082
5. Analysis of the reduction of detent force in a permanent magnet linear synchronous motor / Yoshimura T., Kim H. J., Watada M., Torii S., Ebihara D. // IEEE Transactions on Magnetics. 1995. Vol. 31, Issue 6. P. 3728–3730. doi: https://doi.org/10.1109/20.489752
6. Gieras J. F. Linear induction Drives. Oxford University press Inc., 1994.
7. Zhu Z. Q., Howe D. Instantaneous magnetic field distribution in brushless permanent magnet DC motors. III. Effect of stator slotting // IEEE Transactions on Magnetics. 1993. Vol. 29, Issue 1. P. 143–151. doi: https://doi.org/10.1109/20.195559
8. Lim J., Jung H.-K. Cogging force reduction in permanent magnet linear motor using phase set shift // 2008 18th International Conference on Electrical Machines. 2008. doi: https://doi.org/10.1109/icelmach.2008.4800188
9. An Analytical Method for predicting Cogging Forces in Linear Induction motors / Rusli M., Moscrop J., Platt D., Cook C. // LDIA. 2011. P. 301–307.
10. Rusli M., Cook C. Design of geometric parameters of a double-sided linear induction motor with ladder secondary and a consideration for reducing cogging force // ARPN Journal of Engineering and Applied Sciences. 2015. Vol. 10, Issue 15. P. 6319–6328.
11. The Effect of Ladder-Bar Shape Variation for A Ladder-Secondary Double-Sided Linear Induction Motor (LSDSLIM) Design to Cogging Force and Useful Thrust Performances / Rusli M., Wardana I. N. G., Choiron M. A., Muslim M. A. // Journal of Telecommunication, Electronic and Computer Engineering. 2018. Vol. 8, Issue 1-9. P. 87–92.
12. Design, Manufacture and Finite Element Analysis of a Small-Scale Ladder-Secondary Double-Sided Linear Induction Motor / Rusli M., Wardana I. N. G., Choiron M. A., Muslim M. A. // Advanced Science Letters. 2017. Vol. 23, Issue 5. P. 4371–4377. doi: https://doi.org/10.1166/asl.2017.8853
13. Calibration and compensation of cogging effect in a permanent magnet linear motor / Mu H.-H., Zhou Y.-F., Wen X., Zhou Y.-H. // Mechatronics. 2009. Vol. 19, Issue 4. P. 577–585. doi: https://doi.org/10.1016/j.mechatronics.2008.12.004
14. A New Cogging-Free Permanent-Magnet Linear Motor / Youn S. W., Lee J. J., Yoon H. S., Koh C. S. // IEEE Transactions on Magnetics. 2008. Vol. 44, Issue 7. P. 1785–1790. doi: https://doi.org/10.1109/tmag.2008.918921
15. Reduction of cogging force in slotless linear permanent magnet motors / Zhu Z. Q., Xia Z. P., Howe D., Mellor P. H. // IEE Proceedings – Electric Power Applications. 1997. Vol. 144, Issue 4. P. 277. doi: https://doi.org/10.1049/ip-epa:19971057

16. Design of Linear Induction Drives by Field Analysis and Finite-Element Techniques / Dawson G. E., Eastham A. R., Gieras J. F., Ong R., Ananthasivam K. // IEEE Transactions on Industry Applications. 1986. Vol. IA-22, Issue 5. P. 865–873. doi: https://doi.org/10.1109/tia.1986.4504805
17. Comparative investigation of rotary and linear motor feed drive systems for high precision machine tools / Brandenburg G., Bruckl S., Dormann J., Heinzl J., Schmidt C. // 6th International Workshop on Advanced Motion Control Proceedings. 2000. doi: https://doi.org/10.1109/amc.2000.862898
18. El-Rahman A. The Effect of skewing on Torque Pulsations in a slip-Ring Induction Motor with Stator Voltage Control // Electric Energy Conference 1987: An International Conference on Electric Machines and Drives; Proceedings. Barton, ACT: Institution of Engineers, 1987. P. 458–461.

Дослідження було проведено для визначення впливу двох факторів на електроосадження плівок $Ni(OH)_2$: концентрації нітрату нікелю в електроліті і наявністю операції сушіння між отриманням плівки і її електрохімічними і оптичними випробуваннями. Для осадження використовували чисті розчини нітрату нікелю без добавок, щоб наявність останніх не ускладнювала аналіз одержуваних даних.

В результаті були отримані дві серії плівок з електролітів, які містять різні концентрації нітрату нікелю 0,01, 0,1 та 1 М. Відмінністю двох серій була відсутність або наявність операції сушіння після отримання. Сушіння плівок проводили в м'яких умовах при кімнатній температурі.

Електрохімічні та оптичні властивості визначали методом циклічної вольтамперометрії з паралельним записом зміни прозорості плівок.

В результаті аналізу отриманих даних було з'ясовано, що рівномірні плівки з приблизно однаковою товщиною можуть бути одержані в інтервалі концентрацій нітрату нікелю від 0,01 до 0,1 М. У розчинах, які містять 1 М нітрат нікелю, осадження відбувалося вкрай нерівномірно. Автори запропонували гіпотезу, згідно з якої така поведінка системи пояснюється перерозподілом густини струму по площі електрода через високу електропровідності концентрованого розчину нітрату нікелю. У свою чергу перерозподіл густини струму призводило до багаторазового підвищення густини струму у поверхні електроліт – повітря. Таке підвищення могло впливати на фронт реакції, який віддалявся від електрода або осадженням $Ni(OH)_2$ з високою товщиною. Останній втрачав контакт з поверхнею електрода і осипався.

У свою чергу було встановлено, що процес сушіння значно впливає на структуру і властивості плівок. Також було показано, що процес сушіння негативно впливає на візуальний вигляд плівок гідроксиду нікелю через утворення сітки тріщин на електроді. На додачу до цього, було припущено, що гідроксид нікелю отриманий електрохімічним шляхом містить велику кількість кристалізаційної води

Ключові слова: $Ni(OH)_2$, гідроксид нікелю, електрохромізм, NiOOH, плівка, електроосадження, циклічна вольтамперометрія, концентрація, нітрат нікелю

UDC 544.653.1
DOI: 10.15587/1729-4061.2019.162572

OPTIMIZATION OF THE DEPOSITION CONDITIONS FOR $Ni(OH)_2$ FILMS FOR ELECTROCHROMIC ELEMENTS OF "SMART" WINDOWS

V. Kotok
PhD, Associate Professor
Department of Processes, Apparatus and General Chemical Technology*
E-mail: valeriykotok@gmail.com
PhD, Senior Researcher
Competence center
"Ecological technologies and systems"**
V. Kovalenko
PhD, Associate Professor
Department of Analytical Chemistry and Chemical Technologies of Food Additives and Cosmetics*
E-mail: vadimchem@gmail.com
PhD, Senior Researcher
Competence center
"Ecological technologies and systems"**
*Ukrainian State University of Chemical Technology
Gagarina ave., 8, Dnipro, Ukraine, 49005
**Vyatka State University
Moskovskaya str., 36, Kirov, Russian Federation, 610000

1. Introduction

Electrochromism is a phenomenon characterized by a reversible change in light absorbance (transmittance) of material under applied electrical current. The phenomenon was discovered more than 50 years ago [1, 2]. Nevertheless, real working prototypes of devices utilizing electrochromism only now started to appear [3, 4]. This is related to difficulties in implementing such systems, which in turn are determined by necessary requirements to them. These requirements are more strict than for other systems. Electrochromic materials that are based on electrochemical reactions are required to have a large working life cycle, stability over time and under different temperatures, while also having high